Improving T_2-Weighted Imaging at High Field Through the Use of k_T-Points

Florent Eggenschwiler,[1] Kieran R. O'Brien,[2] Rolf Gruetter,[1,2,3] and José P. Marques[3]

Purpose: At high magnetic field strengths ($B_0 \geq 3$ T), the shorter radiofrequency wavelength produces an inhomogeneous distribution of the transmit magnetic field. This can lead to variable contrast across the brain which is particularly pronounced in T_2-weighted imaging that requires multiple radiofrequency pulses. To obtain T_2-weighted images with uniform contrast throughout the whole brain at 7 T, short (2–3 ms) 3D tailored radiofrequency pulses (k_T-points) were integrated into a 3D variable flip angle turbo spin echo sequence.
Methods: The excitation and refocusing "hard" pulses of a variable flip angle turbo spin echo sequence were replaced with k_T-point pulses. Spatially resolved extended phase graph simulations and in vivo acquisitions at 7 T, utilizing both single channel and parallel-transmit systems, were used to test different k_T-point configurations.
Results: Simulations indicated that an extended optimized k-space trajectory ensured a more homogeneous signal throughout images. In vivo experiments showed that high quality T_2-weighted brain images with uniform signal and contrast were obtained at 7 T by using the proposed methodology.
Conclusion: This work demonstrates that T_2-weighted images devoid of artifacts resulting from B_1^+ inhomogeneity can be obtained at high field through the optimization of extended k_T-point pulses. **Magn Reson Med 71:1478–1488, 2014. © 2013 Wiley Periodicals, Inc.**

Key words: T_2-weighted imaging; B_1^+ inhomogeneity correction; k_T-points; TSE sequence

T_2-weighted imaging is a widely used MRI technique for the diagnosis of brain diseases involving gray matter (GM) and white matter (WM) lesions such as multiple sclerosis. T_2-weighted imaging should benefit from the increased signal-to-noise ratio available at high field strengths ($B_0 \geq 3$ T) to allow higher spatial resolution acquisitions and hence better visualization of small brain structures. However, when moving toward ultra-high field, the increased resonance frequency of proton nuclei causes the radiofrequency (RF) wavelength to become smaller than the typical sample size, leading to an inhomogeneous distribution of the transmit magnetic field (B_1^+). This spatial B_1^+ inhomogeneity gives rise not only to variations in signal intensity for a given tissue across the brain, but more importantly, to different degrees of T_1 or T_2 contrast between two tissues as has been shown in literature (1–3). In particular, fluid attenuation inversion recovery (FLAIR) imaging (2,3), which is one of the most efficient techniques for highlighting contrast between GM and WM, and double inversion recovery (DIR) imaging (1), which is widely used for GM visualization in multiple sclerosis, could be significantly improved by correcting the nonuniform B_1^+ profile observed at 7 T and its propagation into the signal evolution of the involved turbo spin echo (TSE) sequence.

Adiabatic pulses have long been proposed as a means to reduce the sensitivity to transmit field inhomogeneities. It was shown that they can flip/invert/refocus the magnetization as expected even in the presence of substantial B_1^+ inhomogeneities (4). Unfortunately, adiabatic pulses result in a much larger specific absorption rate (SAR) than amplitude modulated RF pulses. This limitation becomes even more prominent at higher field strengths.

Parallel transmission, where each element of an array coil can be driven independently, provides a new degree of freedom that can be used to mitigate B_1^+ inhomogeneity. The simplest methodology to take advantage of such hardware is to perform RF-shimming (5), which seeks to optimize the amplitude and phase of each array element, while keeping the waveforms unchanged, in order to reach a targeted B_1^+ distribution over the sample. RF-shimming has been used in the context of T_2-weighted imaging at 3 T to reduce the B_1^+ field inhomogeneity by using either global or varying RF-shimming combinations throughout a TSE train (6).

Another promising method for B_1^+ inhomogeneity correction consists of designing short RF pulses applied at different locations in k-space and with different RF amplitudes. This weighted k-space trajectory represents yet another new degree of freedom for improving B_1^+ homogeneity. An even higher flexibility for the B_1^+ correction can be reached by combining this approach with parallel transmission (7,8), which allows the design of independent weightings of the k-space trajectory for each transmit channel of the array coil.

For slab selection, the gradient waveforms are chosen so that the k-space trajectory covers a number of k_z segments at different k_x-k_y locations or k-spokes (9). For nonselective excitation, the k-space trajectory is designed to cover a number of discrete points in k-space referred as k_T-points, as proposed by Cloos et al. (10). Promising results have previously shown that k-spokes can be designed to produce a homogeneous excitation profile across a 2D field of view (FOV) (9,11–13) and equivalently in 3D, k_T-points were shown to provide highly

homogenous excitation (10) and inversion profiles throughout the entire brain, giving rise to high quality T_1-weighted images at 7 T (14).

The aim of this article is to demonstrate that k_T-points can be used to significantly improve the homogeneity observed in nonselective 3D T_2-weighted imaging at 7 T. The T_2-weighted images were acquired with a commercially available variable flip angle TSE sequence known as the sampling perfection with application optimized contrasts using different flip angle evolutions (SPACE) sequence (15). This sequence optimizes the signal evolution of the flip angle train for specified T_1/T_2 relaxation times and allows longer RF-pulse trains to be utilized. At high field strengths, the inhomogeneous B_1^+ distribution makes the expected signal evolution of a specific tissue position dependent, leading to contrast variations throughout the image. The TSE sequence's nonselective hard pulses were replaced by k_T-point pulses designed based on the subject's acquired B_1^+ map to improve the excitation profile homogeneity and remove the spatial dependent contrast in T_2-weighted images. Herein, we show that the use of k_T-point pulses for both excitation and refocusing of the signal on a single channel transmit system and a parallel-transmit (PTx) system can improve the T_2-weighted imaging quality.

METHODS

k_T-Points and RF Pulse Design

The k_T-points were designed by making use of the small-tip-angle (STA) approximation (16), which allows the three-dimensional excitation profile after an RF pulse to be written as a Fourier transform expression involving a weighted k-space trajectory.

Based on the transmit sensitivity of the RF coil transmitting in circularly polarized (CP) mode (single channel system) or of each transmit coil element (PTx system), the positions and weights of N k_T-points were optimized in order to obtain the most homogeneous excitation profile, by considering a magnitude least squares approach (17).

The magnitude of the designed excitation profile was optimized because in many imaging applications, the phase profile of the final image is relatively unimportant, provided it is only slowly varying from one voxel to the next (18).

To find the N k_T-point locations, a modified version of the sequential optimal selection of spokes (SOLO) algorithm (19) was implemented. The first k_T-point was fixed at $\mathbf{k} = \mathbf{0}$ and the subsequent k_T-points were searched on a 3D grid covering the following k-space locations: $k_x \in [-3\Delta k_x; +3\Delta k_x]$, $k_y \in [-3\Delta k_y; +3\Delta k_y]$, $k_z \in [-2\Delta k_z; +2\Delta k_z]$, where the grid steps $\Delta k_{x,y,z} = 1/FOV_{x,y,z}$. This set of low spatial frequencies was selected because only smooth variations in the brain's B_1^+ profiles are observed at 7 T. For each k_T-point to be added, the SOLO algorithm fixes the previously determined k_T-points and evaluates each of the remaining positions of the grid. For each trial, the amplitudes and phases of the RF sub-pulses related to the involved k-space locations are optimized according to a local phase-exchange method (20). The k-space location providing the excitation profile the closest to the targeted one is kept and the next algorithm

iteration begins. The algorithm stops when all the N desired k_T-points are found.

The optimization was performed for the voxels belonging to a 3D mask designed by applying Brain Extraction Toolbox (www.fmrib.ox.ac.uk) on a gradient echo (GRE) image used to calculate the coil transmit sensitivity.

When designing k_T-points on the PTx system, one particular set of RF weights was optimized for each coil element and Lagrangian multipliers, λ, were introduced to penalize the amount of RF power deposited, taking into account the fact that different channels had different forward and reflected power which made the SAR constraint to be channel dependent. A first estimation of the per channel sequence power was obtained from the RF power monitoring units of the PTx system when running the sequence with a short repetition time (TR), low-resolution and without k_T-point pulse. Based on those values, the power per channel of the desired protocol with k_T-point pulses was calculated for each coil element. As long as all the computed power per channel values were not below a pre-computed threshold, the sub-pulses were redesigned by iteratively increasing the Lagrangian multipliers related to elements exceeding the limit.

The resulting k_T-point pulse consists of a set of RF sub-pulses and gradient blips corresponding to the weighted k-space trajectory designed by the SOLO algorithm. This k_T-point pulse is then used to replace the nonselective hard pulses in the TSE sequence in order to correct the effects of the B_1^+-inhomogeneity in the resulting T_2-weighted images.

k_T-Point Pulse Implementation and Evaluation

The SOLO algorithm, being based on the STA approximation, has no information regarding the order in which the different k-space locations should be visited. Given that the TSE sequence uses pulses with flip angles beyond the range for which the STA approximation is valid, two types of sub-pulse sets were designed to replace the original pulses of the TSE sequence (cf. Fig. 1a). The first approach consisted in creating pulses with N sub-pulses corresponding to the N k-space positions found by the SOLO algorithm, similarly to what is usually presented in literature (10,19,21,22). Half of the sub-pulses were applied before the sub-pulse at $\mathbf{k} = \mathbf{0}$ and the remaining were applied after it (cf. Fig. 1b). Because it contains most of the RF energy, the sub-pulse exciting k-space center was fixed at half of the RF pulse duration in order to guarantee a refocusing of the signal halfway through the duration separating the refocusing pulses of the TSE sequence. Such a k_T-point pulse made of N sub-pulses corresponds to the fastest way of exciting the optimized k-space trajectory and will be referred to as a "short k_T-point pulse." In the second approach, the sub-pulse exciting the $\mathbf{k} = \mathbf{0}$ position was also forced at the center of the trajectory for the same reason as for the short k_T-point pulse, and the remaining sub-pulses were split around it with their durations halved (cf. Fig. 1c). In this way, the optimized k-space trajectory is visited twice with a total of $2N - 1$ sub-pulses applied for an N k_T-points design. Halving the duration of the sub-pulses applied at $\mathbf{k} \neq \mathbf{0}$ locations was performed so that the
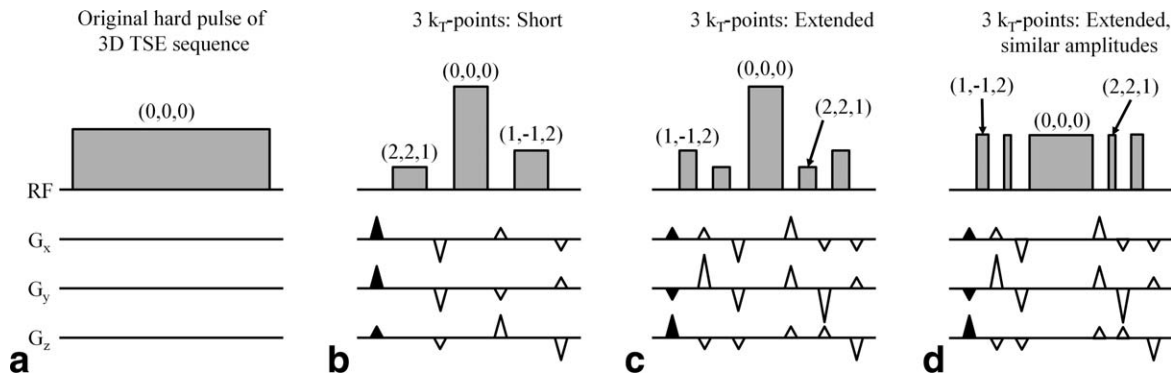
FIG. 1. Types of RF pulse shapes for which performance analysis of the TSE sequence was realized. **a**: Original hard pulse exciting k-space center position. **b**: Short k_T-point pulse exciting the k-space trajectory defined by: $\mathbf{k_1} = (2, 2, 1)^T \cdot 1/FOV$; $\mathbf{k_2} = (0, 0, 0)^T \cdot 1/FOV$; $\mathbf{k_3} = (1, -1, 2)T \cdot 1/FOV$, with FOV = $(FOV_x, FOV_y, FOV_z)^T$ mm^3. The positions $\mathbf{k_1}$ and $\mathbf{k_3}$ were arbitrarily chosen for the example purpose. The large central pulse is applied at $\mathbf{k} = 0$. Other sub-pulses correspond to the other k-space positions found by the SOLO algorithm. **c**: Extended k_T-point pulse exciting the same trajectory as for the short k_T-point pulse. For both short and extended k_T-point pulses, CPMG conditions are fulfilled because each positive gradient blip is compensated by a negative one. **d**: Same extended k_T-point pulse as in (c) with reshaped sub-pulse amplitudes and durations in order to minimize the pulse SAR. Having the sub-pulse amplitudes similar across the whole pulse makes the energy deposition more efficient.

excitation profile can be kept close to the one resulting from the STA approximation for longer by reducing the rotation associated with each sub-pulse, while allowing most of the energy to be delivered in the center of the RF pulse and hence have the refocusing of the MR signal still at the center of the echo spacing. As its duration is increased in respect to the short k_T-point pulse and its excitation profile should be closer to the STA approximation in a larger range of flip-angles, this pulse will be referred to as an "extended k_T-point pulse."

In TSE sequences, several types of echoes (primary echo, stimulated echo, etc.) arise from multiple refocusing mechanisms. It is fundamental that the phases of simultaneously acquired echoes are coherent in order to avoid signal-to-noise ratio degradation and image artifacts (23). To ensure that the multiple echoes of the TSE sequence occur at the desired time points with phase consistency, the Carr Purcell Meiboom Gill (CPMG) conditions (23–25) must be fulfilled throughout the entire train of flip angles.

The second condition requires the gradient moments between two successive RF pulses of the sequence to be balanced. Hence, gradient blips (solid triangles in Fig. 1b,c) were added for each type of pulse at the start in order to fulfill this property. This ensures that the k-space trajectory is correctly visited according to the backward time-relationship presented in (26) stating that the k-space trajectory always finishes at $\mathbf{k} = \mathbf{0}$, but also that it starts from the $\mathbf{k} = \mathbf{0}$ position (only relevant for the refocusing pulses).

Triangular gradient blips with 300 T/m/s slew rate were used in this work. Given that the k_T-point locations correspond to low spatial frequencies, the gradient blip durations were of 50–150 μs.

To determine the best strategy between short and extended k_T-point pulses, Bloch simulations of the excitation profiles provided by both methods were performed for a range of flip angles going from $45°$ to $120°$, which

encompasses the range of RF pulses applied in the TSE sequence. For those simulations, equilibrium initial magnetization $\mathbf{M} = (M_x, M_y, M_z)^T = (0, 0, 1)^T$ was assumed. The excitation profiles $e(\mathbf{r})$ were calculated in the following way:

$$e(\vec{r}) = \tan^{-1}\left(\frac{M_{xy}(\vec{r})}{M_z(\vec{r})}\right) \cdot \frac{1}{\alpha^{nom}} e^{i\angle M_{xy}(\vec{r})} \qquad [1]$$

such that $|e(\mathbf{r})|$ represents a multiplicative factor of a nominal flip angle α^{nom}. M_{xy} and M_z correspond to the states of transverse and longitudinal magnetizations at the end of the pulse.

To further evaluate the different k_T-point implementations and their similarity to the STA regime, full Bloch simulations were additionally calculated for five different subjects and four types of k_T-point pulses: short N (N k_T-points—N sub-pulses, Fig. 1b); extended N (N k_T-points—$2N - 1$ sub-pulses, Fig. 1c); short $2N - 1$ ($2N - 1$ k_T-points—$2N - 1$ sub-pulses); extended N asymmetric (N k_T-points—$2N - 1$ sub-pulses with the $\mathbf{k} = \mathbf{0}$ sub-pulse applied at the end of the waveform). The third waveform (short $2N - 1$) was introduced to guarantee that the improvements observed were not simply due to the increased number of sub-pulses, but by effectively reducing their tip. The last waveform was analyzed to determine if having a certain form of symmetry was an important feature when designing a unique set of k_T-points for the excitation and refocusing pulses of the sequence (even if frequency evaluation was not considered during the RF pulse). The deviation between full Bloch equation profile and the excitation profile resulting from the STA approximation, STA($\mathbf{r}$) was calculated as $||(e(\mathbf{r}) - STA(\mathbf{r}))/STA(\mathbf{r})||_1$ for different flip-angles ($10°$ to $120°$ in steps of $10°$). All the possible arrangements of the sub-pulses applied at $\mathbf{k} \neq \mathbf{0}$ locations for each of the five different subjects were considered in this analysis.

Turbo Spin Echo Sequence Simulation with Spatially Resolved Extended Phase Graph

To evaluate the impact of introducing k_T-points in the TSE sequence, the signal throughout the sequence was simulated using the extended phase graph formalism (description presented in (27)). This methodology presents the advantage that it describes the full Bloch equations with a relatively low computational demand. The B_1^+ profile and the designed k_T-points were taken into account in the signal calculation, which means that each flip angle of the TSE sequence becomes position dependent. A similar model, the spatially resolved extended phase graph (SR-EPG), which considers spatially varying flip angles throughout a TSE sequence was proposed in (6). Full Bloch simulations of the magnetization evolution throughout the TSE sequence were thus performed by using this model. To ensure that magnetization reaches steady state, the sequence was simulated over 5·TR periods. The signal acquired at echo time (TE) was calculated for 5 subjects for the case of : (a) hard pulses (Fig. 1a); (b) short 3 k_T-point pulses (Fig. 1b); (c) extended 3 k_T-point pulses (Fig. 1c); (d) short 5 k_T-point pulses; (e) extended 3 k_T-point asymmetric pulses. The deviation from the theoretical EPG signal (assuming perfectly homogeneous B_1^+ field) was computed similarly to what was described in the previous section.

Experimental Setup

In vivo scans were performed on a Siemens 7 T scanner (Siemens Healthcare, Germany) with parallel transmission capabilities and equipped with a head gradient insert (maximum gradient amplitude and slew rate of 80 mT/m and 333 T/m/s, respectively). A 32 channel coil (Nova Medical, USA) was used when transmitting RF signals in combined mode (single channel system), whereas a custom-designed eight-channel transmit-receive array coil (RAPID Biomedical, Germany) was used for parallel transmission (PTx system).

The experimental protocol was approved by local ethics committee and two healthy subjects providing informed consent were scanned. For subject's safety, simulations of the eight-channel transmit-receive array were performed for the use of PTx system and the worst case scenario (sum of in phase electric fields over the whole brain) implied that the maximum power delivered by each coil element was limited to 0.9 W/10 s and 0.3 W/6 min.

B_1^+-Mapping Protocol

When using the single channel system, the transmit sensitivity profile was obtained by acquiring an absolute B_1^+ map of the subject's brain using the SA2RAGE sequence (28) with the following parameters: TR = 2.4 s, TE = 1.35 ms, delay times $TD_1 = 50$ ms and $TD_2 = 1800$ ms, $\alpha_1 = 4°$, $\alpha_2 = 11°$, $3.2 \times 3.2 \times 4.0$ mm^3 resolution, and a $64 \times 64 \times 48$ matrix size acquired with sagittal orientation (acquisition time of 1 min 28 s).

With the PTx system, the transmit sensitivity profiles of every array elements were required. To find those profiles an absolute B_1^+ map was acquired using the

SA2RAGE sequence with the same protocol as that used for the single channel system and array elements transmitting with channel phases defined such that constructive interferences occur at the brain center (SA2RAGE^{All}). 3D-GRE measurements with a protocol equivalent to the SA2RAGE sequence in terms of TE, resolution, and bandwidth were performed (remaining parameters TR = 3.5 ms, $\alpha_1 = 1°$, acquisition time of 11 s). One 3D-GRE acquisition was made with all array elements transmitting (GRE^{All}) and the phase configuration identical to the one used for the SA2RAGE sequence. Subsequently, in order to excite eight array modes, eight 3D-GRE sequences were acquired with the same phase configuration but with one of the transmitting elements off (GRE$^{AllButOne}_m$, where m refers to the nontransmitting channel). The absolute B_1^+ profiles of the different modes were computed as:

$$B_{1,m}^+ = \text{SA2RAGE}^{All} \frac{\text{GRE}_m^{AllButOne}}{\text{GRE}^{All}} \qquad [2]$$

To be able to estimate the interference between B_1^+ maps of different coils, it is fundamental to know both magnitude and phase of B_1^+. The phase of transmit field was assumed to be simply equal to that of the GRE images, although it also includes B_0 field inhomogeneities and reception B_1^- phase contributions, as these are the same for all the measured maps their contribution to the interference can be neglected. $B_1^+(\boldsymbol{r})$ was therefore assumed to be equal to $|B_1^+(\boldsymbol{r})|e^{i\cdot\varphi(\boldsymbol{r})}$, where φ is the GRE phase and $|B_1^+|$ corresponds to the value calculated in Eq. [2]. Individual coil profiles were finally computed by matrix inversion (29).

Turbo Spin Echo Protocol

Replacing the original hard pulses of the TSE sequence with variable flip angles by sets of sub-pulses and gradients blips increases the SAR of the sequence, which is especially problematic when using the PTx system for which the SAR limits are more restrictive. As a consequence, the duration of these pulses had to be longer than would have been necessary using simple hard pulses. This inherently affected the echo spacing (and hence TE) of the sequence and the calculation of the flip angle train. To keep the comparison simple and limited to the change of the homogeneity of the excitation profile, and not to TEs and different flip angle trains, the same pulse length was used with and without k_T-points. While this might have affected the maximum signal and contrast achieved by the TSE sequence when using hard pulses, it should not have affected the homogeneity of the contrast throughout the brain. The following protocols were used in the different systems:

i. Single channel system: TR = 1 s, TE = 313 ms, echo train length (ETL) = 120, echo spacing (ES) = 5.68 ms, RF duration (RF$_{Dur}$) = 2.11 ms, resolution = $0.8 \times 0.8 \times 0.8$ mm^3, matrix size = $320 \times 320 \times 208$, and 4 k_T-points per RF pulse (total acquisition time of 4 min 15 s);

ii. PTx system: TR = 6 s, TE = 460 ms, ETL = 120, ES = 7.66 ms, RF$_{Dur}$ = 3.08 ms, resolution = $0.75 \times 0.75 \times$
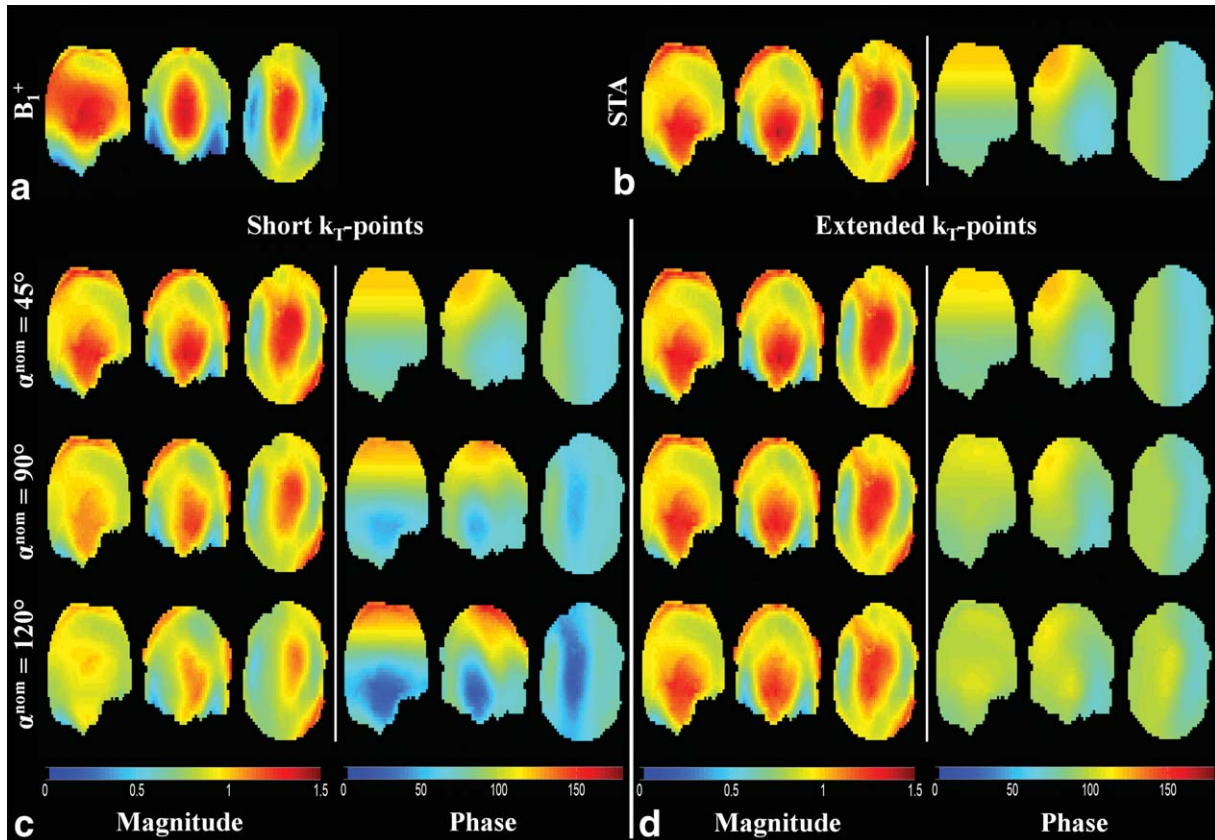
FIG. 2. **a**: B_1^+ profiles of a particular subject acquired using the SA2RAGE sequence. **b**: Magnitude and phase of the excitation profile expected from the STA approximation. Alternatively, excitation profiles calculated by full Bloch simulations of (**c**) short k_T-point (Fig. 1b) and (**d**) extended k_T-point (Fig. 1c) pulses related to the design of 3 k_T-points in the single channel system, performed based on the B_1^+ profiles in (a). The range of flip angles simulated in (c) and (d) roughly corresponds to the one used for the train of refocusing pulses on the TSE sequence.

0.85 mm³, matrix size $= 256 \times 256 \times 176$, and 3 k_T-points per RF pulse (total acquisition time of 13 min 08 s).

As the role of the first refocusing pulses is mainly to lead the magnetization toward steady-state and the signal associated to them has much higher amplitude than that of the steady-state, the echoes occurring in the beginning of the refocusing train were not used for image reconstruction. For the protocols used on the single channel and PTx systems, 15 and 20 echoes were, respectively, discarded at the beginning of the train.

On both systems, a standard TSE image with identical parameters and nonselective hard pulses of the same duration as the k_T-point pulses was also acquired for comparison.

Data Processing

To focus on the improvement provided by k_T-points in terms of contrast and signal homogeneity, bias field correction was subsequently applied to the anatomical images acquired on the single channel system, in order to remove the signal variations related to the highly non-uniform reception profile $B_1^-(\mathbf{r})$ of the 32 channel coil. The bias field correction was performed using FMRIB's automated segmentation tool (www.fmrib.ox.ac.uk)

which calculates a smooth profile, mainly corresponding to $B_1^-(\mathbf{r})$ (30).

This processing step was not applied on images acquired on the PTx system because an acceptable homogeneity was observed for the B_1^- profile of the eight channel array coil. The TSE images resulting from this correction were visually compared with the uncorrected ones.

RESULTS

k_T-Point Implementation and Evaluation

Designing the k_T-point pulses based on the B_1^+ profiles resulting from the SA2RAGE acquisition (Fig. 2a), leads to the STA approximation maps (Fig. 2b) that were compared with the full Bloch simulations of the excitation profiles related to the short and extended k_T-point pulses (cf. Fig. 2c,d), performed for different flip angles. The simulated magnitude and phase of the excitation profiles $e(\mathbf{r})$ after the pulse, given by Eq. [1] are displayed for each type of pulse. Figure 2c shows that both magnitude and phase of the excitation profiles involving a short k_T-point pulse start to diverge from the STA approximation solution when simulating large flip angles ($>60°$). This observation can be explained by the fact that such flip angles are out of the regime where the STA
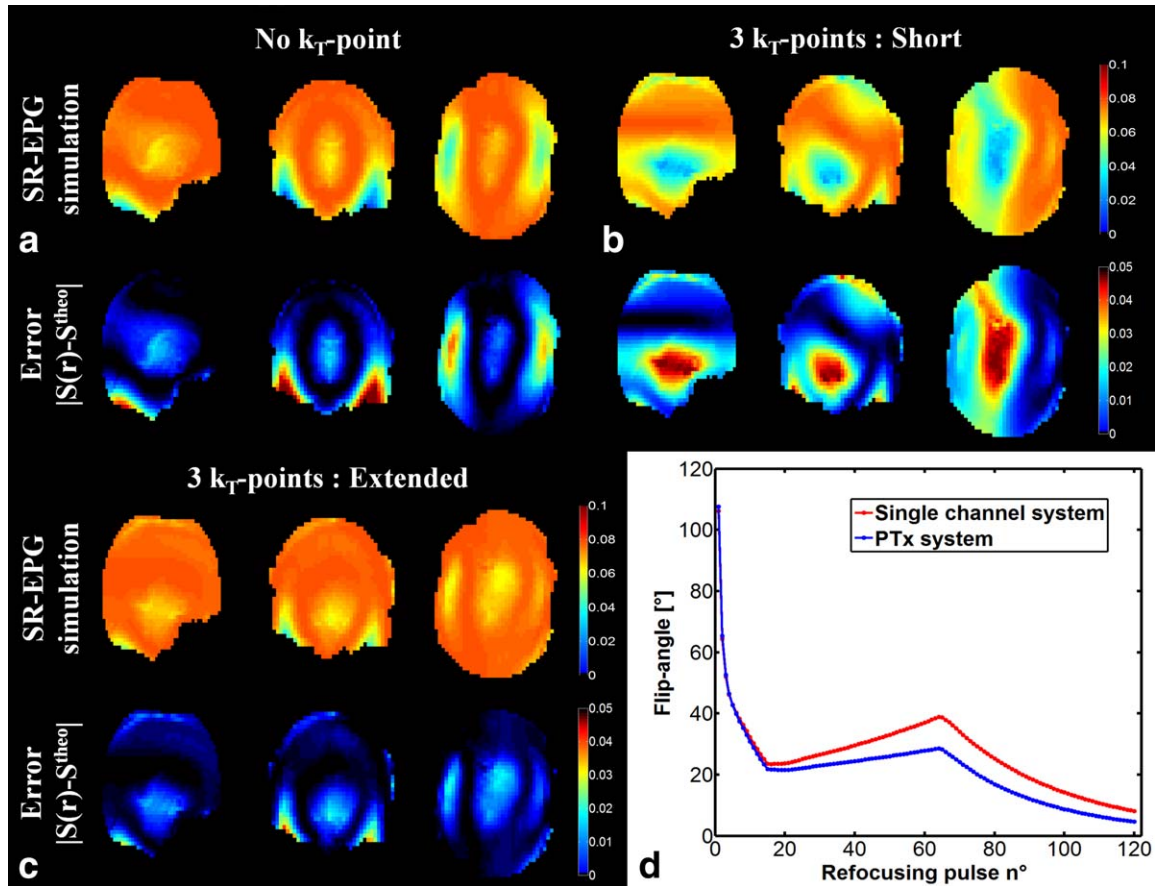
FIG. 3. Signal coming from the central k-space acquisition calculated with SR-EPG simulations of the TSE sequence for a particular subject. The signal maps calculated by using (**b**) short (Fig. 1b) and (**c**) extended (Fig. 1c) 3 k_T-point pulses in the sequence were compared with the profiles simulated without k_T-point (**a**). The second row in (a), (b), and (c) displays the profiles of the absolute value of the difference between images of the first row $S(\mathbf{r})$ and the theoretical signal at k-space center S^{theo} calculated assuming a perfectly homogeneous B_1^+ distribution across the brain. **d**: Flip angle train for the TSE sequence when using the protocols presented in the "Methods" section for the single channel system (red curve) and for the PTx system (blue curve). [Color figure can be viewed in the online issue, which is available at wileyonlinelibrary.com.]

approximation holds, as described in (31,32). However, with an extended k_T-point pulse, Figure 2d demonstrates that the excitation profiles remain remarkably close to the STA approximation solution even when simulating flip angles as high as 120°.

Figure 3 shows SR-EPG simulations of the TSE sequence for both types of k_T-point pulses considered (Fig. 3b,c). For comparison, the profiles simulated without k_T-point are also displayed (Fig. 3a). The sequence parameters presented in the "Methods" section for the single channel system were used for those simulations. On Figure 3a–c, the first row shows the TSE signal for a tissue of $T_1/T_2 = 1.5$ s/75 ms simulated after the 55th refocusing pulse (k-space center) for each voxel within the region of interest. On the second row, the difference between the profiles of the first row and the theoretical signal at k-space center calculated with the standard extended phase graph simulation (assuming a perfectly homogeneous B_1^+ distribution) is presented.

The flip angle values for the train of refocusing RF pulses throughout the TSE sequence corresponding to

the protocol used for the single channel (red curve) and PTx (blue curve) systems are presented in Figure 3d.

The profiles presented in Figure 3 confirm the higher quality of the results obtained when using an extended k_T-point pulse. Comparing the mean of the error maps of both types of pulses (cf. second row of Fig. 3a–c), it is possible to conclude that the extended k_T-point pulse outperforms the short k_T-point pulse by more than 60% in terms of signal homogeneity obtained in the final image. This difference is mainly due to high flip angles of the refocusing pulses present at the beginning of the train (cf. Fig. 3d) where the deviation from the STA approximation varies significantly depending on which pulse is used (cf. last row of Fig. 2c,d). Moreover, the severe phase variation observed between the last two rows of Figure 2c, means that when using short k_T-point pulses in the TSE sequence, for many voxels, the CPMG conditions (23) are violated between the excitation and refocusing pulses and between high flip angle refocusing pulses. This phase discrepancy leads to a higher inhomogeneity (Fig. 3b) of the signal maps than that obtained when using standard hard pulses (Fig. 3a), especially in
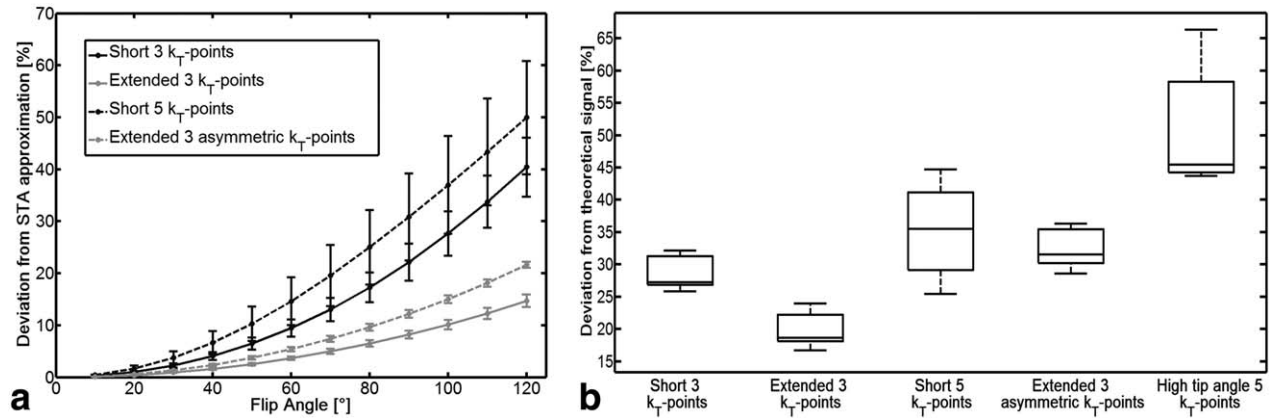
FIG. 4. **a**: Plot of the deviation between excitation profile corresponding to full Bloch simulations of an RF pulse and the excitation profile of the STA approximation as a function of the flip angle. Four different pulses are shown: a short 3 k_T-point pulse (solid black); an extended 3 k_T-point pulse (solid gray); a short 5 k_T-point pulse (dashed black); an extended asymmetric 3 k_T-point pulse (dashed gray). For each type, all the configurations of the sub-pulses corresponding to off-centered k-space positions were simulated for five different subjects. Each point represents the average and standard deviation (given by error bars) over the subjects and sub-pulse configurations. **b**: Box-and-whisker diagrams of the deviation between the theoretical signal and the SR-EPG simulations for five different subjects. On the x-axis, the different tested pulse configurations are shown. Additionally to the four trajectories and waveforms in (a), the results for a pulse designed based on the extended 3 k_T-point pulse, and optimized on the high tip angle regime to offer homogeneous $60°$ excitation are shown.

regions exhibiting large variations in the phase profiles of Figure 2c. The high stability in the phase profiles of the extended k_T-point pulse (see Fig. 2d) suggests that the validity of CPMG conditions is extended up to a larger flip angle range as is supported by SR-EPG simulations (Fig. 3c).

To further support the results of Figure 2, the deviations from the STA regime of four different k_T-point waveforms are displayed in Figure 4a. Comparing the curves related to short and extended k_T-point pulses in Figure 4a clearly confirms that the excitation profile stays closer to that of the STA approximation when exciting with the extended k-space trajectory. The same conclusion can be arrived at by comparing the curves corresponding to the extended 3 k_T-point pulse and the short 5 k_T-point pulse, which are both pulses made of 5 sub-pulses. This observation suggests that the improvement is not due simply to the number of sub-pulses of the k_T-point waveforms but to effectively reducing the rotation associated with each sub-pulse. Figure 4b emphasizes that extended k_T-point pulses perform better than short k_T-point pulses not only for excitation but also when used as refocusing pulses. The deviation between the theoretical signal profile (perfectly homogeneous B_1^+) and the one simulated by considering k_T-points is smaller for an extended 3 k_T-point pulse than for a short 5 k_T-point pulse, despite the fact that the latter provides a more homogenous excitation profile in the STA regime. The extended 3 k_T-point waveform with the sub-pulse associated to $\mathbf{k}=\mathbf{0}$ position applied at the end showed acceptable excitation properties (Fig. 4a) but was worse than both the short and extended 3 k_T-point pulses on the SR-EPG simulations (Fig. 4b). This shows that having the large sub-pulse exciting k-space center in the middle of the RF shape is important not only from

an echo formation point of view but also to guarantee a better refocusing capability of the k_T-point pulse. Finally, a k_T-point waveform was designed in the high tip angle regime (32–34) using a gradient descent method over the Bloch simulations, starting from the extended 3 k_T-point solution. An homogeneous excitation profile was targeted for a $60°$ flip angle (roughly corresponding to the average flip angle of the first ramp of the echo train in Fig. 3d) and the k-space trajectory was kept the same as for the extended 3 k_T-point pulse (optimization of the sub-pulses only). Although the excitation profile homogeneity of the high tip angle RF shape outperformed the one of the extended 3 k_T-point pulse by 30% in terms of std/mean, Figure 4b shows that using such a pulse to replace the pulses of the TSE sequence had the worst outcome in terms of TSE signal homogeneity. This can be explained by the fact that homogeneity in the excitation profile obtained for a $60°$ k_T-point pulse (which is optimal) rapidly deteriorates for other flip angle values.

The set of sub-pulses and gradients used to replace the original hard pulses of the TSE sequence on the single channel system are displayed in Figure 1d (example with $N=3$). The sub-pulses in Figure 1c were distributed over the predefined total pulse duration (RF_{Dur}) in a way minimizing the SAR of the k_T-point pulse. A 29% SAR drop was observed when comparing the pulses of Figure 1c,d. The sub-pulse amplitudes were finally weighted according to the flip angles of the excitation pulse and the refocusing pulse train (cf. Fig. 3d). This was also performed on the PTx system, where one specific set of sub-pulses was designed for each array element.

On the single channel and PTx systems, the use of k_T-points, respectively, comes at the cost of an 8- and 3-fold increase in global SAR when compared with an hard pulse with the same total duration meaning that the RF
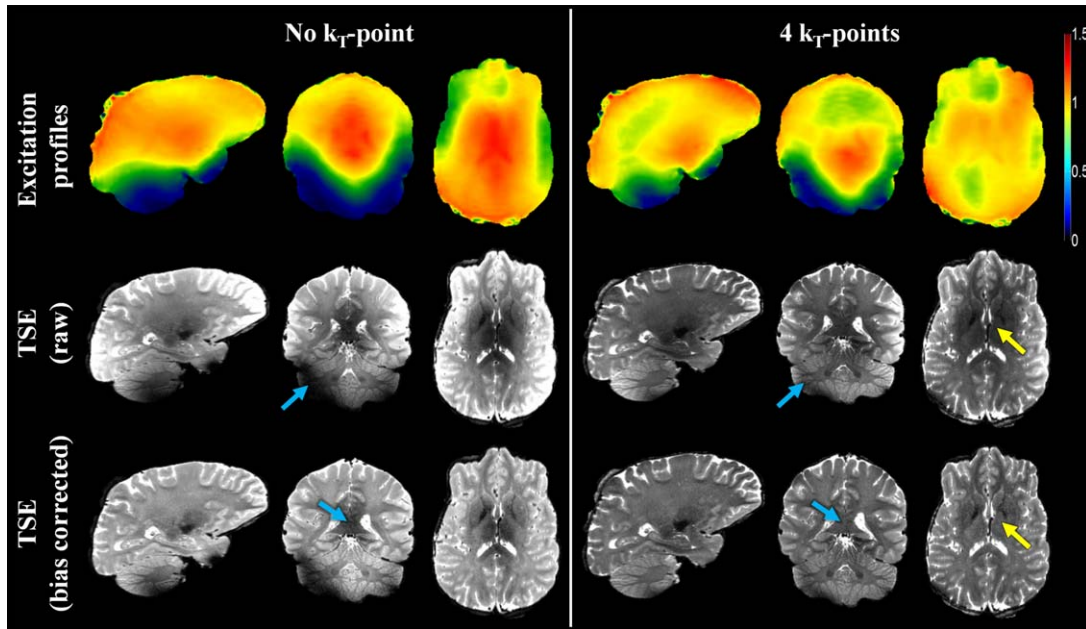
FIG. 5. Excitation profiles and TSE images obtained with (right columns) and without (left columns) the use of 4 k_T-points on the single channel system. The k_T-points were designed to correct the inhomogeneous excitation profile measured at 7 T using the SA2RAGE sequence. The second row shows raw TSE images that subsequently underwent bias field correction (third row) using FMRIB's automated segmentation tool. Blue arrows highlight areas where signal homogeneity was highly improved. Yellow arrows emphasize the fact that residual signal variations observed on images acquired using k_T-points are dominated by the receive field nonuniformity. [Color figure can be viewed in the online issue, which is available at wileyonlinelibrary.com.]

pulse used had to be adapted to have a length, respectively, $\sim$3 and $\sim$2 times bigger than that would be possible when using standard hard pulses.

Excitation Profiles and TSE Images

Excitation profiles simulated with and without 4 k_T-points for the single channel system are presented in the first row of Figure 5. The corresponding TSE images are displayed on the following rows. The second row presents the raw TSE images, whereas the third one shows TSE profiles subjected to bias field correction. Using 4 k_T-points improves the predicted excitation profile homogeneity which leads to less signal variation for a given tissue across the brain. Considerable improvement occurs in the cerebellum and in the central brain region (blue arrows) both prior to and post bias field corrections. The darker region still observable in the brain center when 4 k_T-points are used (yellow arrows) is significantly reduced when using bias field correction demonstrating that it is most likely to be due to the receive coil profiles (B_1^-). On the other hand, the contrast observed in this region (close to the thalamus) in the absence of k_T-point, remains even after bias field correction. This region of low intensity is correlated with regions of high B_1^+ field and not to anatomical contrast (as can be observed by its extension to the corpus callosum). Some dark areas still persist on the bias field corrected images of the right columns. Those regions are correlated with the remaining low intensity regions of the corrected excitation profile.

Figure 6 shows the results obtained on the PTx system (8 channels) when 3 k_T-points are designed. Blue arrows point out regions that are severely affected by the inhomogeneity in the original excitation profile and for which the improvement provided by the k_T-points is most relevant. On the middle row, the arrows highlight the intensity asymmetry between the left and right hippocampus observed in the absence of k_T-point and corrected after using k_T-points. In the bottom row, a magnified view over the top-right area of the axial slices through the temporal lobe highlights the lack of contrast between GM and WM, which is recovered by designing 3 k_T-points (blue arrows). Also the signal intensity in the WM surrounding the red nucleus and substantia nigra is significantly increased with the proposed methodology. Throughout the TSE images acquired with k_T-points, it is possible to observe that regions of low intensity reflect (as expected) structures known to be iron rich such as the dentate nucleus in the cerebellum, the red nucleus and substantia nigra in the brain stem, subthalamic nuclei, and the globus pallidus (green arrows). On the other hand, in the absence of k_T-point regions of low intensity can also be attributed to the high and low nominal B_1^+ values visible on the excitation profiles.

DISCUSSION

This study shows that T_2-weighted images, known to be highly affected by the inhomogeneous distribution of the B_1^+ field observed at 7 T (1–3), can be considerably improved by replacing the original hard pulses of a TSE
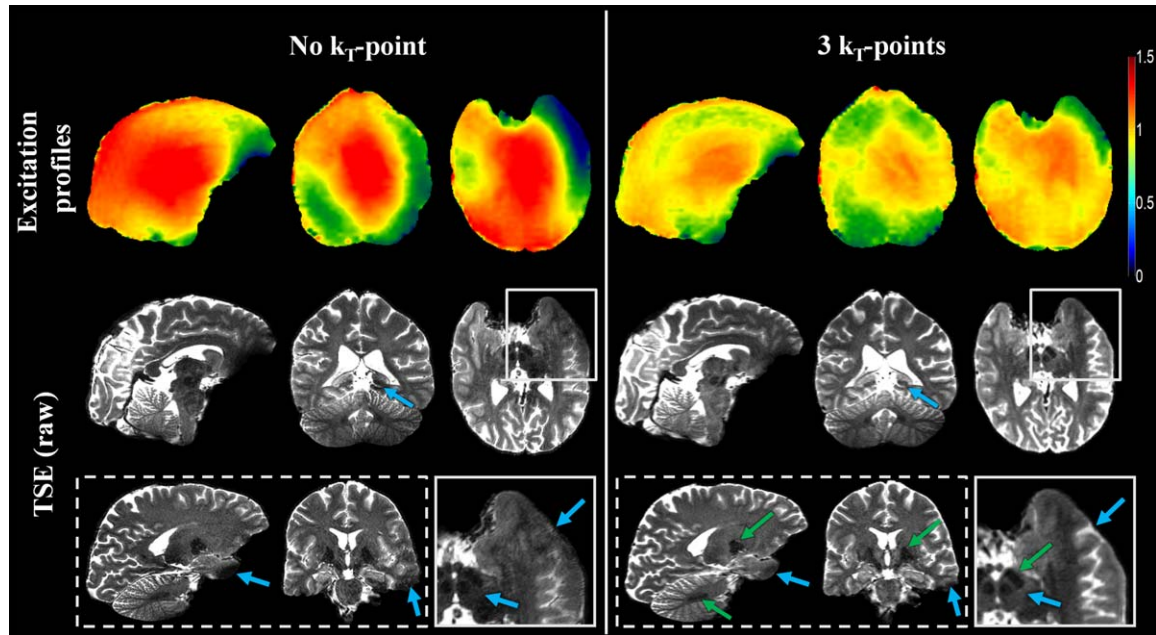
FIG. 6. Excitation profiles and TSE images obtained without (left columns) and with (right columns) the use of 3 k_T-points on the PTx system. Raw TSE images are presented in the second and third rows. Solid boxes: Zooms over the top-right area of the axial profiles presented in the second row. Improved GM-WM contrast is clearly observed in the temporal lobe in the inset corresponding to the anatomical image acquired by using 3 k_T-points. Dashed boxes: Sagittal and coronal views of the raw TSE images for slices different from the ones presented in the second row. Blue arrows highlight brain parts for which signal homogeneity was highly improved, whereas green arrows point out the fact that structures known to be iron rich are clearly distinguishable on the TSE images acquired using k_T-points. [Color figure can be viewed in the online issue, which is available at wileyonlinelibrary.com.]

sequence with variable flip angles by k_T-point pulses. It was also demonstrated that exciting the optimized k-space trajectory multiple times with a reduced rotation associated to the sub-pulses applied at the off-center k-space locations, extends the validity of the STA approximation up to flip angles as high as $120°$.

The comparison of short and extended k_T-point pulses was performed according to their excitation properties (transfer of M_z toward M_{xy}) in Figures 2 and 4a. The same examination could also be conducted for the other transfer pathways, e.g., refocusing (M_{xy} toward M_{xy}^*, where M_{xy}^* is the complex conjugate of M_{xy}). This was implicitly done when simulating the signal using the SR-EPG framework, see Figures 3 and 4b, which takes all the transfer pathways into account. The homogeneity observed for the TSE profiles resulting from the use of extended k_T-point pulses thus means that this type of pulse is better suited for all transfer pathways (excitation and refocusing). From the previous discussion, it can be concluded that: the design of a unique set of k_T-points for the pulses of a TSE sequence highly benefits from exciting the optimized k-space trajectory twice (with the RF energy of the sub-pulses applied at off-center k_T-points halved). It should be emphasized though that, independently of the argument of echo formation at the center of the echo spacing (the SR-EPG did not consider frequency evolution during the RF pulses), symmetry in the extended k_T-point waveforms (large sub-pulse in the center of the RF shape) provides a higher degree of homogeneity in the signal calculated (cf. Fig. 4b). The only cost of the extended k_T-point pulse is in the length of the RF pulse (due to the increased number of gradient

blips) that was 9 and 5% longer for the single and pTx systems, respectively.

Designing 4 k_T-points on the single channel system already provided a high degree of homogeneity on the anatomical images (cf. Fig. 5). However, some areas exhibit low signal even after bias field correction. Those areas are highly correlated with the remaining low intensity regions of the excitation profile. To further improve the excitation profile homogeneity, the number of designed k_T-points could be increased. However, to sufficiently correct those low intensity regions, a large number of k_T-points would be needed (data not shown), which would be prohibitive due to both SAR and pulse length limitations. Another approach to obtain a higher homogeneity of the excitation profile when using the single transmit system would be the combination of the proposed method with the use of highly dielectric pads positioned close to the cerebellum (35,36) which can significantly improve the available B_1^+ field in this region. Furthermore, such a methodology that increases the strength of the B_1^+ field in regions where it is currently virtually absent will have a positive impact in terms of SAR (as it will decrease the amplitude of the various sub-pulses).

Designing k_T-points combined with parallel transmission further improved the homogeneity of the excitation profile throughout the brain and consequently the quality of TSE images (cf. Fig. 6). Despite the fact that different RF coils and subjects were used, it can be nevertheless observed that the excitation profiles obtained with the PTx system outperformed those of the single channel system even when using a smaller number of k_T-points and despite the need to use

regularization parameters to minimize the delivered power. Note that due to higher SAR restrictions on the PTx system, a less SAR-intensive protocol of the TSE sequence (lower refocusing pulses; cf. Fig. 3d) and a 6-fold longer repetition time were used. In the future, using methodologies recently proposed to monitor the local SAR deposition based on various body models (37,38), and additionally incorporate the design of the k_T-point waveform (39) and different regularization parameters for the different channels (40) should allow the SAR limits to be relaxed, and more efficient protocols to be used.

Although B_0-shimming was performed on both single channel and PTx systems to reduce the B_0 inhomogeneity effects, TSE images acquired using k_T-points are still affected by the residual B_0 nonuniformity, for example in Figure 6 where a darker signal is observed in the frontal lobe region. This effect is more pronounced on the images acquired with the PTx system due to the reduced bandwidth of the 3.08 ms RF-pulses used throughout the sequence. Such artifacts could be minimized either by designing shorter k_T-point pulses (at the cost of an SAR increase), or by mapping the B_0 field distribution across the brain and considering it in the pulse designing procedure (31,41). Another source of errors in the RF-pulse design procedure can arise from inaccuracy of the B_1^+ maps used. Indeed, the precision with which the transmit field is measured decreases on low B_1^+ regions (42). On the single channel system, this limitation can be overcome by increasing the B_1^+ field on those regions, either with the use of a higher RF voltage or, as mentioned earlier, with the utilization of highly dielectric pads (36). On the PTx system, the B_1^+ maps related to individual coil elements were calculated by combining an absolute B_1^+ measurement with eight individual relative B_1^+ maps (obtained from different modes via matrix inversion, cf. "Methods" section). The limitation of this approach is that inaccuracies in regions with low values in the quantitative B_1^+ maps will be amplified when the low B_1^+ values are of destructive interference origin (the ratio of GRE images for various channels in Eq. [2] is greater than one). This can significantly affect the individual coil profiles. A possible solution would be to repeat the B_1^+-mapping procedure (both quantitative and relative measurements) by using a phase combination such that constructive interferences occur at the regions presenting low values on the first absolute B_1^+ acquisition. A matrix inversion taking both datasets into account would thus provide individual B_1^+ profiles with improved quality. It is hence possible that the inhomogeneity on some regions was not corrected to its full capacity because the B_1^+ field used in the pulse design algorithm was not accurately measured (for example, in the temporal lobe).

In this article, a unique set of N k_T-points was optimized for all the RF pulses of the TSE sequence and the STA approximation was used throughout although pulses as high as $120°$ were used in the protocols. The next step for improving further the quality of T_2-weighted imaging will be to design separate k_T-points for the excitation and for the refocusing pulses, the ultimate goal being to optimize a k_T-point waveform for each pulse of the TSE sequence. To this end, the methodology presented in (6) would be of particular interest because instead of optimizing the excitation profile, it directly models and optimizes the signal throughout the TSE sequence with the SR-EPG framework. As in this framework, all transitions are already described by a full Bloch equation formalism, the outcome will not be sensitive to deviation from the STA regime which could further improve the quality of the resulting T_2-weighted images. More importantly, such an increase of the degrees of freedom could allow the usage of shorter and less SAR intensive k_T-point pulses allowing more efficient protocols to be used.

CONCLUSIONS

We conclude that replacing the original hard pulses of the TSE sequence by one set of sub-pulses exciting an optimized k-space trajectory provides T_2-weighted images of high quality in terms of signal and contrast homogeneity. Combining this methodology with parallel transmission gives access to anatomical images largely devoid of artifacts resulting from the common B_1^+ inhomogeneity at 7 T. The methodology presented here could be extended to FLAIR and DIR imaging because those techniques only require the addition of a magnetization preparation module based on adiabatic pulses prior to the excitation and could find applications in the study or diagnosis of brain diseases involving GM and WM lesions such as multiple sclerosis and iron deposition such as Alzheimer disease.

REFERENCES

1. Madelin G, Oesingmann N, Inglese M. Double inversion recovery MRI with fat suppression at 7 tesla: initial experience. J Neuroimaging 2010;20:87–92.
2. Visser F, Zwanenburg JJ, Hoogduin JM, Luijten PR. High-resolution magnetization-prepared 3D-FLAIR imaging at 7.0 Tesla. Magn Reson Med 2010;64:194–202.
3. Zwanenburg JJ, Hendrikse J, Visser F, Takahara T, Luijten PR. Fluid attenuated inversion recovery (FLAIR) MRI at 7.0 Tesla: comparison with 1.5 and 3.0 Tesla. Eur Radiol 2010;20:915–922.
4. Garwood M, DelaBarre L. The return of the frequency sweep: designing adiabatic pulses for contemporary NMR. J Magn Reson 2001;153: 155–177.
5. Hoult DI, Phil D. Sensitivity and power deposition in a high-field imaging experiment. J Magn Reson Imaging 2000;12:46–67.
6. Malik SJ, Padormo F, Price AN, Hajnal JV. Spatially resolved extended phase graphs: modeling and design of multipulse sequences with parallel transmission. Magn Reson Med 2012;68:1481–1494.
7. Katscher U, Bornert P, Leussler C, van den Brink JS. Transmit SENSE. Magn Reson Med 2003;49:144–150.
8. Zhu Y. Parallel excitation with an array of transmit coils. Magn Reson Med 2004;51:775–784.
9. Saekho S, Yip CY, Noll DC, Boada FE, Stenger VA. Fast-kz three-dimensional tailored radiofrequency pulse for reduced B_1 inhomogeneity. Magn Reson Med 2006;55:719–724.
10. Cloos MA, Boulant N, Luong M, Ferrand G, Giacomini E, Le Bihan D, Amadon A. kT-points: short three-dimensional tailored RF pulses for flip-angle homogenization over an extended volume. Magn Reson Med 2012;67:72–80.
11. Setsompop K, Alagappan V, Gagoski B, et al. Slice-selective RF pulses for in vivo B_1+ inhomogeneity mitigation at 7 tesla using parallel RF excitation with a 16-element coil. Magn Reson Med 2008;60: 1422–1432.
12. Setsompop K, Alagappan V, Zelinski AC, Potthast A, Fontius U, Hebrank F, Schmitt F, Wald LL, Adalsteinsson E. High-flip-angle

slice-selective parallel RF transmission with 8 channels at 7 T. J Magn Reson 2008;195:76–84.

13. Zelinski AC, Wald LL, Setsompop K, Alagappan V, Gagoski BA, Goyal VK, Adalsteinsson E. Fast slice-selective radio-frequency excitation pulses for mitigating B_1^+ inhomogeneity in the human brain at 7 Tesla. Magn Reson Med 2008;59:1355–1364.

14. Cloos MA, Boulant N, Luong M, Ferrand G, Giacomini E, Hang MF, Wiggins CJ, Le Bihan D, Amadon A. Parallel-transmission-enabled magnetization-prepared rapid gradient-echo T_1-weighted imaging of the human brain at 7 T. Neuroimage 2012;62:2140–2150.

15. Mugler JP. Three-dimensional T2-weighted imaging of the brain using very long spin-echo trains. In Proceedings of the 8th Annual Meeting of ISMRM, Denver, Colorado, USA, 2000. p. 687.

16. Hoult DI. Solution of the Bloch equations in the presence of a varying B_1 field—approach to selective pulse analysis. J Magn Reson 1979;35:69–86.

17. Setsompop K, Wald LL, Alagappan V, Gagoski BA, Adalsteinsson E. Magnitude least squares optimization for parallel radio frequency excitation design demonstrated at 7 Tesla with eight channels. Magn Reson Med 2008;59:908–915.

18. Kassakian P. Magnitude least-squares fitting via semidefinite programming with applications to beamforming and multidimensional filter design. Int Conf Acoust Speech 2005;3:53–56.

19. Ma C, Xu D, King KF, Liang ZP. Joint design of spoke trajectories and RF pulses for parallel excitation. Magn Reson Med 2011;65:973–985.

20. Kassakian P. Convex approximation and optimization with applications in magnitude filter design and radiation pattern synthesis, PhD Thesis. Berkeley: University of California; 2006.

21. Setsompop K, Alagappan V, Gagoski BA, Potthast A, Hebrank F, Fontius U, Schmitt F, Wald LL, Adalsteinsson E. Broadband slab selection with B-1(+) mitigation at 7 T via parallel spectral-spatial excitation. Magn Reson Med 2009;61:493–500.

22. Zelinski AC, Wald LL, Setsompop K, Goyal VK, Adalsteinsson E. Sparsity-enforced slice-selective MRI RF excitation pulse design. IEEE Trans Med Imaging 2008;27:1213–1229.

23. Bernstein MA, King KF, Xiaohong JZ. Handbook of MRI pulse sequences. Burlington, MA: Elsevier Academic Press; Burlington, MA, 2004.

24. Carr HY, Purcell EM. Effects of diffusion on free precession in nuclear magnetic resonance experiments. Phys Rev 1954;94:630–638.

25. Meiboom S, Gill D. Modified spin-echo method for measuring nuclear relaxation times. Rev Sci Instrum 1958;29:688–691.

26. Pauly J, Nishimura D, Macovski A. A K-space analysis of small-tip-angle excitation. J Magn Reson 1989;81:43–56.

27. Scheffler K. A pictorial description of steady-states in rapid magnetic resonance imaging. Concept Magn Res 1999;11:291–304.

28. Eggenschwiler F, Kober T, Magill AW, Gruetter R, Marques JP. SA2RAGE: a new sequence for fast B_1^+-mapping. Magn Reson Med 2012; 67:1609–1619.

29. Brunner DO, Pruessmann KP. $B_1(+)$ interferometry for the calibration of RF transmitter arrays. Magn Reson Med 2009;61:1480–1488.

30. Zhang Y, Brady M, Smith S. Segmentation of brain MR images through a hidden Markov random field model and the expectation-maximization algorithm. IEEE Trans Med Imaging 2001;20:45–57.

31. Grissom W, Yip CY, Zhang Z, Stenger VA, Fessler JA, Noll DC. Spatial domain method for the design of RF pulses in multicoil parallel excitation. Magn Reson Med 2006;56:620–629.

32. Xu D, King KF, Zhu Y, McKinnon GC, Liang ZP. Designing multichannel, multidimensional, arbitrary flip angle RF pulses using an optimal control approach. Magn Reson Med 2008;59:547–560.

33. Grissom WA, Yip CY, Wright SM, Fessler JA, Noll DC. Additive angle method for fast large-tip-angle RF pulse design in parallel excitation. Magnet Reson Med 2008;59:779–787.

34. Pauly J, Nishimura D, Macovski A. A linear class of large-tip-angle selective excitation pulses. J Magn Reson 1989;82:571–587.

35. Teeuwisse WM, Brink WM, Haines KN, Webb AG. Simulations of high permittivity materials for 7 T neuroimaging and evaluation of a new barium titanate-based dielectric. Magn Reson Med 2012;67: 912–918.

36. Teeuwisse WM, Brink WM, Webb AG. Quantitative assessment of the effects of high-permittivity pads in 7 Tesla MRI of the brain. Magn Reson Med 2012;67:1285–1293.

37. Eichfelder G, Gebhardt M. Local specific absorption rate control for parallel transmission by virtual observation points. Magn Reson Med 2011;66:1468–1476.

38. Graesslin I, Homann H, Biederer S, Bornert P, Nehrke K, Vernickel P, Mens G, Harvey P, Katscher U. A specific absorption rate prediction concept for parallel transmission MR. Magn Reson Med 2012;68: 1664–1674.

39. Lee J, Gebhardt M, Wald LL, Adalsteinsson E. Local SAR in parallel transmission pulse design. Magn Reson Med 2012;67:1566–1578.

40. Cloos MA, Luong M, Ferrand G, Amadon A, Le Bihan D, Boulant N. Local SAR reduction in parallel excitation based on channel-dependent Tikhonov parameters. J Magn Reson Imaging 2010;32:1209–1216.

41. Brunner DO, Pruessmann KP. Optimal design of multiple-channel RF pulses under strict power and SAR constraints. Magn Reson Med 2010;63:1280–1291.

42. Pohmann R, Scheffler K. A theoretical and experimental comparison of different techniques for $B(1)$ mapping at very high fields. NMR Biomed 2013;26:265–275.